tvst

Article

Automatic Localization of the Scleral Spur Using Deep Learning and Ultrasound Biomicroscopy

Wensai Wang[1], Lingxiao Wang[1], Tao Wang[1], Xiaochun Wang[1], Sheng Zhou[1], Jun Yang[1], and Song Lin[2]

[1] Institute of Biomedical Engineering, Chinese Academy of Medical Sciences and Peking Union Medical College, Tianjin, China
[2] Eye Institute and School of Optometry, Tianjin Medical University Eye Hospital, Tianjin, China

Correspondence: Song Lin, Eye Institute and School of Optometry, Tianjin Medical University Eye Hospital, 251 Fukang Rd, Tianjin 300384, People's Republic of China. e-mail: linsong123123@sina.com
Jun Yang, Institute of Biomedical Engineering, Chinese Academy of Medical Sciences and Peking Union Medical College, 236 Baidi Rd, Tianjin 300192, People's Republic of China. e-mail: yangj3210@hotmail.com

Received: February 4, 2021
Accepted: July 26, 2021
Published: August 24, 2021

Keywords: deep learning; ultrasound biomicroscopy; scleral spur; automatic localization

Citation: Wang W, Wang L, Wang T, Wang X, Zhou S, Yang J, Lin S. Automatic localization of the scleral spur using deep learning and ultrasound biomicroscopy. Transl Vis Sci Technol. 2021;10(9):28, https://doi.org/10.1167/tvst.10.9.28

Purpose: The purpose of this study was to develop a convolutional neural network (CNN) for automated localization of the scleral spur in ultrasound biomicroscopy (UBM) images of open-angle eyes.

Methods: UBM images were acquired, and one glaucoma specialist provided reference coordinates of scleral spur locations in all images. A CNN model based on the EfficientNetB3 architecture was developed to detect the scleral spur in each image. The prediction errors and Euclidean distance were used to evaluate localization performance of the CNN model. Trabecular-iris angle 500 (TIA500) and angle-opening distance 500 (AOD500) were measured and analyzed using the scleral spur locations provided by the specialist and predicted by the CNN model.

Results: The CNN was developed using a training dataset of 2328 images and tested using an independent dataset of 258 images. The mean absolute prediction errors of CNN model were 48.06 $\pm$ 45.40 µm for X-coordinates and 30.84 $\pm$ 27.03 µm for Y-coordinates. The mean absolute intraobserver variability was 47.80 $\pm$ 44.45 µm for X-coordinates and 29.50 $\pm$ 25.77 µm for Y-coordinates. The mean Euclidean distance of the CNN was 60.41 $\pm$ 49.02 µm and the intraobserver mean Euclidean distance was 59.78 $\pm$ 47.12 µm. The mean absolute error in TIA500 was 1.26 $\pm$ 1.38 degrees for all test images and in AOD500 was 0.039 $\pm$ 0.051 mm.

Conclusions: A CNN can detect the scleral spur on UBM images of open-angle eyes with performance similar to that of a glaucoma specialist.

Translational Relevance: Deep learning algorithms for automating scleral spur localization would facilitate the quantitative assessment of the opening of the angle and the risk in angle closure.

Introduction

Gonioscopy is the clinical standard for evaluating the anterior chamber angle (ACA).[1,2] However, gonioscopy assessments are subjective, qualitative, and depends on the examiner's clinical experience.[3] Ultrasound biomicroscopy (UBM) is a noninvasive imaging technique that is not affected by optical media opacities and has intense penetration through ocular tissues.[4–6] UBM images provide quantitative assessments of the opening of the angle and the ocular biometric parameters. In light of these significant advantages, UBM has been widely used in the clinical examination of several ophthalmic diseases, especially angle closure glaucoma.[7,8]

Angle-closure is a significant risk factor for primary angle-closure glaucoma (PACG).[9–11] In open-angle eyes, quantitative assessments of the opening of the angle can monitor the progression of angle narrowing and angle-closure over time, which helps diagnose and manage angle-closure glaucoma and other angle-closure diseases. Trabecular-iris angle (TIA) and angle-opening distance (AOD) are typical parameters in the quantitative assessment of the opening of the angle.[12,13] However, UBM image analysis is

semi-automated, and the operator must first identify the specific anatomic structure before quantifying the opening of the angle.

The scleral spur is a crucial anatomic marker for the assessment of the opening of the angle. The accurate localization of the scleral spur is fundamental in the precise measurement of TIA and AOD. It also presents a difficulty in the measurement process, which usually requires the operator to have rich clinical experience and imaging knowledge. However, in the case of UBM images with low signal noise and edge blur, which is a common finding, the judgment of the position of the scleral spur highly relies on the manual detection of the scleral spur, and this affects the positioning accuracy of the scleral spur to a certain extent due to the subjective differences among ophthalmologists. Even in some automated measurement methods, such as the one reported by Leung et al. to automatically measure TIA and AOD based on UBM images,[14] the scleral spur's location needs to be manually determined. Therefore, a credible and accurate automatic localization method for the sclera spur is of great significance for the automatic quantitative assessment of the opening of the angle and the risk in angle closure.

With the development of artificial intelligence, the intelligent processing algorithm of medical images based on deep learning has made continuous progress in ophthalmology, proving the effectiveness of deep learning.[15–18] In this study, we develop a convolutional neural network (CNN) for automated localization of the scleral spur in UBM images of open-angle eyes.

Methods

According to the World Medical Association's Declaration of Helsinki, the work was carried out and approved by the Ethics Committee of Tianjin Medical University Eye Hospital (2019KY-24).

Dataset

The dataset used in this study was acquired using UBM (MD-300L; MEDA Co. Ltd, Tianjin, China; 50-MHz transducer) between May 2014 and June 2020 at the Tianjin Medical University Eye Hospital (Tianjin, China). The glaucoma specialist (Song Lin) and two of his colleagues captured UBM images from various directions according to clinical needs. These ophthalmologists have more than 8 years of clinical experience and have been trained according to a uniform operating procedure before acquiring images to minimize deviations between examiners. The UBM examination was performed under normal room lighting conditions, the illumination of which was not measured, but bright lights were avoided. UBM images were acquired with the probe and was oriented perpendicular to the corneoscleral limbus. There were no noticeable differences in the anatomic presentation of the scleral spur in different directions.

Table 1. Demographics of the UBM Dataset

Parameters	Training Dataset	Testing Dataset
No. of patients	1012	258
No. of eyes	1668	258
Age (mean ± SD)	43.98 ± 15.62	44.34 ± 16.79
Sex (M/F)	487/525	121/137
Eye (R/L)	831/837	127/131

UBM images were selected from the database consecutively without regard for the visibility of the scleral spur. One hundred fifty-six images were excluded due to ACA structural abnormalities caused by iridodialysis (55 images), motion artifacts (12 images), or incompleteness (89 images). Two hundred sixteen angle-closure images were also excluded. Angle-closure in UBM images is defined by iridotrabecular contact.[19] In this study, each angle-closure images was judged by a glaucoma specialist based on clinical experience. Because the boundary between the corneoscleral and the iris is blurred in UBM images of angle-closure, it is difficult for even experienced glaucoma specialists to determine the exact location of the scleral spur. Therefore, based on the deep learning classification network, we previously realized the automatic classification of the open-angle and angle-closure of the UBM image (the results have been described in another paper). In this study, we only studied the automatic localization of the scleral spur on the open-angle image as the basis for automatically quantitative assessment of the opening of the angle.

This dataset contained 2586 UBM images from 1926 eyes of 1270 patients, 2328 images were assigned to the training set and 258 images to the test set (Table 1). The test set is one image per patient. The train and test sets were split randomly at the patient's level so that images from a single patient were only included in the test or train sets. This operation is essential to prevent data leakage.

In UBM images, the intersection of the demarcation line between scleral tissue and ciliary body tissue and the extension line of the corneal inner surface is the scleral spur location.[12] A glaucoma specialist (Song Lin) uses Labelme software to manually marked the scleral spur's location in each image (Fig. 1). For images where the scleral spur location was ambiguous,

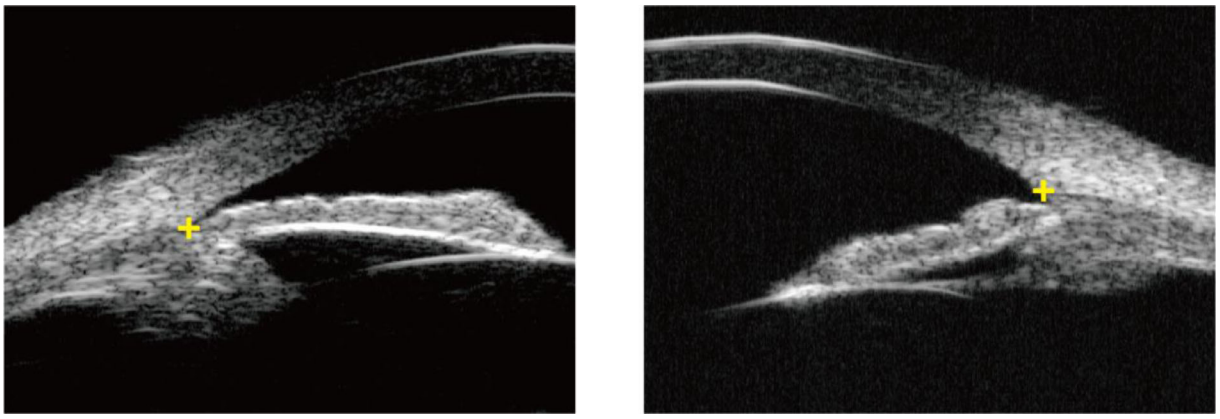

Figure 1. Images were captured by UBM. The UBM examination was performed under normal room lighting conditions; UBM images were acquired with the probe was oriented perpendicular to the corneoscleral limbus. The *left* image shows the temporal side (9 o'clock) of the right eye of one patient, and the *right* image shows the nasal (3 o'clock) side of the right eye of another patient. The *yellow cross* is the scleral spur location marked by glaucoma specialist.

the specialist was encouraged to estimate its location based on clinical experience. These labels of scleral spur locations were used as the reference standard. The specialist marked the test set images for the second time 1 month later. These scleral spur locations were used to calculate intraobserver variability.

Deep Learning Model Development

The CNN model used in this study, a typical U-shaped network structure, including a feature encoder module and a feature decoder module, is shown in Figure 2.

We selected EfficientNetB3 as the feature encoder module for the sclera spur localization model. To satisfy the need for semantic information extraction of sclera spur location, we retained the structure body of EfficientNetB3, removed the final pooling layer, the fully connected layer, and used the 3×3 convolutional layer for further semantic information extraction. The feature decoder module is similar to the feature decoder module of the Unet model. We combined the feature map of the encoding and decoding stages by using skip connection. A 1×1 convolution was used in the final layer to generate heat maps containing the scleral spur's position information.

Gaussian heat maps were generated using the scleral spur's labeled coordinates in UBM images to train the localization model. We used this model to learn the transformation from the UBM image to the Gaussian heat map. We used randomly shifting with 0.2 scales, randomly rotating with 20 degrees, randomly zooming with 0.2 scales, and randomly horizontally flipping as data augmentation. The model was trained with mean square error loss for 200 epochs using Adam optimizer and a batch size of 2. Adam optimizer's learning rate was 0.001 and the decay parameter was set to 0.01 to adjust the learning rate dynamically. The localization implementation is based on the public Keras platform. The training and testing bed is Windows 10 operating system with the GeForce RTX 2080TI graphics cards, which has 12 Gigabyte memory.

Scleral Spur Coordinate Extraction

The localization model's output is a heat map containing the scleral spur's position information, from which the coordinates of the scleral spur are extracted. In this study, we used a coordinate (x_c, y_c) acquisition method based on maximum likelihood estimation, which is defined as follows:

$$x_c = \frac{\sum_{i \in C} x_i p_i}{\sum_{i \in C} p_i} \quad (1)$$

$$y_c = \frac{\sum_{i \in C} y_i p_i}{\sum_{i \in C} p_i} \quad (2)$$

where C represents a set of pixel points whose pixel value is more than half of the maximum pixel value in the heatmap, (x_i, y_i) represents the pixel coordinates, and p_i represents the i^{th} pixel value in C. We, according to the size of the UBM manufacturers to provide a pixel (9.575 µm × 9.575 µm), were able to convert pixel coordinates into micron coordinates.

Deep Learning Model Testing

The scleral spur coordinates marked by the glaucoma specialist were used as the reference coordinates to evaluate the CNN model's overall localization performance.

X- and Y-coordinate prediction errors were calculated by subtracting CNN-predicted coordinates from

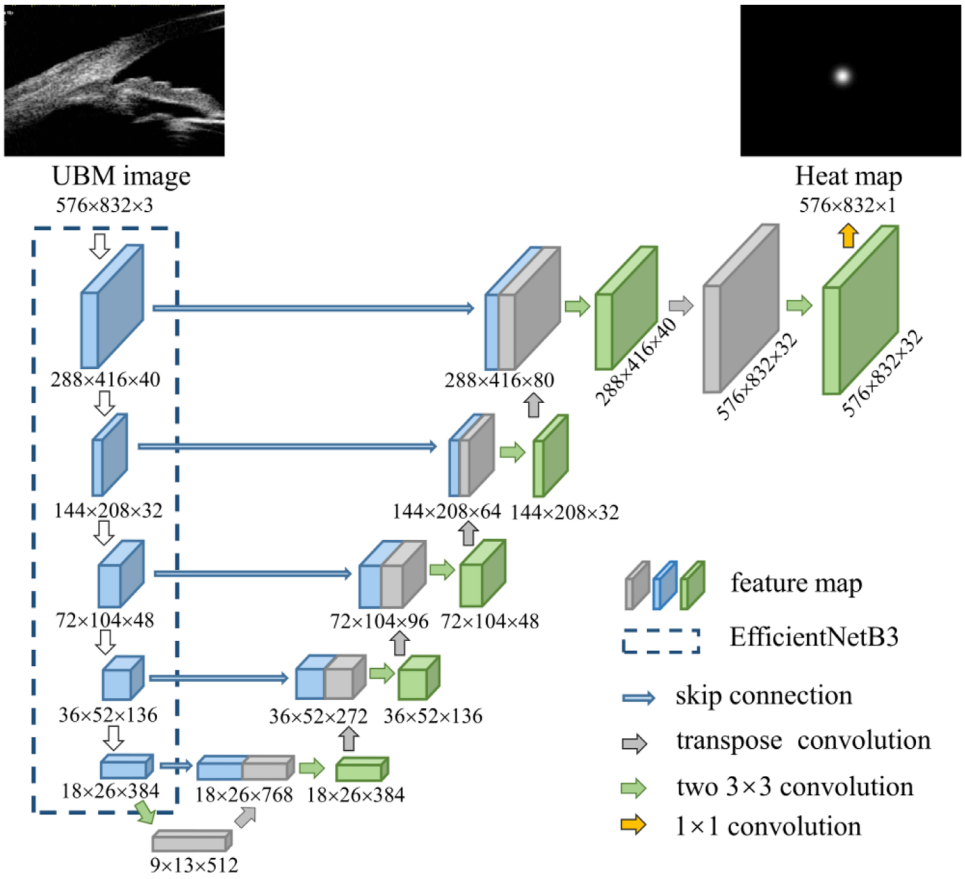

Figure 2. Architecture of the scleral spur localization model.

the corresponding reference coordinates. X- and Y-coordinates' intraobserver errors were calculated by subtracting the second set of scleral spur coordinates by the specialist from corresponding reference coordinates. Euclidean distance was calculated as: $\sqrt{(\text{X-coordinate error}^2 + \text{Y-coordinate error}^2)}$. The normality of X- and Y-coordinate distributions were assessed with the Kolmogorov-Smirnov test. The intraclass correlation coefficient (ICC), assessed by a single grader (absolute agreement and 2-way random effect model) was used to indicate the degree of agreement between scleral spur locations. An ICC value between 0.4 and 0.75 indicates good reproducibility, and more than 0.75 indicates excellent reproducibility.[20] The Mann-Whitney *U* test was used to test for significant differences in localization errors between quadrants.

Calculation of Angle Parameters

According to Pavlin and associates,[12,21,22] TIA500 was defined as an angle measured with the deepest point of the iris recess and the arms passing through the point on the trabecular meshwork 500 µm from the scleral spur and the point on iris anterior surface perpendicularly. AOD500 measured by the length of a line drawn perpendicular to the trabecular meshwork 500 µm from the scleral spur and ending on iris anterior surface. Whereas the specialist marked the scleral spur location on the test set images, the angle recess location and the ACA contour also were marked. We wrote Python programs to automatically calculate TIA500 and AOD500 using the scleral spur locations marked by the expert and predicted by CNN.

Results

The training time of the CNN model was 31 hours, 21 minutes, and 36 seconds, and the testing time for each image in the test set was 102 ms.

Deep Learning Model Performance

The distributions of X- and Y-coordinates were normally distributed (Kolmogorov-Smirnov test, $P > 0.05$). The ICC was calculated for each pair for the X- and Y-coordinates of the scleral spur location (Table 2). The ICC (95% confidence interval [CI])

Table 2. The ICC for the Scleral Spur Location (2-way, Single Score, Absolute Agreement ICC, 95% CI)

X	CNN	M1	M2	Y	CNN	M1	M2
CNN	1	0.996 (0.995–0.997)	0.995 (0.994–0.996)	CNN	1	0.995 (0.993–0.996)	0.994 (0.992–0.995)
M1		1	0.996 (0.995–0.997)	M1		1	0.995 (0.994–0.996)
M2			1	M2			1

X indicates the X-coordinate; Y, Y-coordinate; CNN, the scleral spur localization model; M1, the first marked manually by the specialist (reference standard); M2, the second marked manually by the specialist.

Table 3. The Scleral Spur Localization Error of the CNN Model and Intragrader Variability

	CNN Model Prediction Error (μm)	Intragrader Variability (μm)
X-coordinate	11.32 ± 65.21	6.75 ± 64.99
Y-coordinate	0.63 ± 41.05	0.04 ± 39.22
Absolute X-coordinate	48.06 ± 45.40	47.80 ± 44.45
Absolute Y-coordinate	30.84 ± 27.03	29.50 ± 25.77
Euclidean distance	60.41 ± 49.02	59.78 ± 47.12

Data are expressed as mean ± SD.

of the CNN model was 0.996 (0.995–0.997) for X-coordinates, 0.995 (0.993–0.996) for Y-coordinates. It shows that the coordinates of the scleral spur predicted by the CNN model were in excellent agreement with those by manual marking.

The mean prediction error of the CNN model was 11.32 ± 65.21 μm for X-coordinates and 0.63 ± 41.05 μm for Y-coordinates. The mean absolute prediction error of the CNN model was 48.06 ± 45.40 μm for X-coordinates, 30.84 ± 27.03 μm for Y-coordinates, and 60.41 ± 49.02 μm for Euclidean distance. The mean intra-observer error of scleral spur location was 6.75 ± 64.99 μm for X-coordinates, and 0.04 ± 39.22 μm for Y-coordinates. The mean absolute intra-observer error of scleral spur location was 47.80 ± 44.45 μm for X-coordinates, 29.50 ± 25.77 μm for Y-coordinates, and 59.78 ± 47.12 μm for Euclidean distance (Table 3). As shown in Table 3, although the CNN model prediction error is very close to the intra-observer variabilities, the intragrader variabilities were slightly less than the CNN model prediction error.

The distribution of absolute prediction errors of the CNN was 22.48% within 10 μm, 66.67% within 50 μm, 90.70% within 100 μm, and 96.12% within 150 μm for X-coordinates. The distribution of absolute prediction errors of the CNN was 35.27% within 10 μm, 81.40% within 50 μm, 97.67% within 100 μm, and 99.61% within 150 μm for Y-coordinates. The distribution of Euclidean distance of the CNN was 6.59% within 10 μm, 55.04% within 50 μm, 85.66% within 100 μm, and 95.35% within 150 μm (Fig. 3). Figure 4 shows representative images of various Euclidean distances.

The distribution of absolute errors from intra-observer variability was 19.38% within 10 μm, 68.99% within 50 μm, 91.09% within 100 μm, and 97.29% within 150 μm for X-coordinates. The distribution of absolute errors from intra-observer variability was 32.17% within 10 μm, 84.11% within 50 μm, 98.06% within 100 μm, and 99.61% within 150 μm for Y-coordinates. The distribution of intra-observer Euclidean distance was 6.20% within 10 μm, 52.33% within 50 μm, 87.21% within 100 μm, and 94.96% within 150 μm (see Fig. 3). The distribution of the CNN model prediction error was similar to the distribution of the intragrader variabilities.

The test set showed that 82, 75, 46, and 55 images were acquired in the temporal, nasal, superior, and inferior quadrants, respectively. The mean Euclidean distance of the scleral spur localization model at the temporal, nasal, superior and inferior quadrants was 57.03 ± 47.70 μm, 63.65 ± 48.15 μm, 58.90 ± 45.22 μm, and 62.62 ± 55.68 μm, respectively, as shown in Table 4.

The distribution of localization errors (Euclidean distance) in each quadrant was not normally distributed (Kolmogorov-Smirnov test, $P < 0.05$). Therefore, the Mann-Whitney U test was used to test for significant differences in localization errors between quadrants. We found no statistically significant difference in localization error between each quadrant (Mann-Whitney U test, $P > 0.05$).

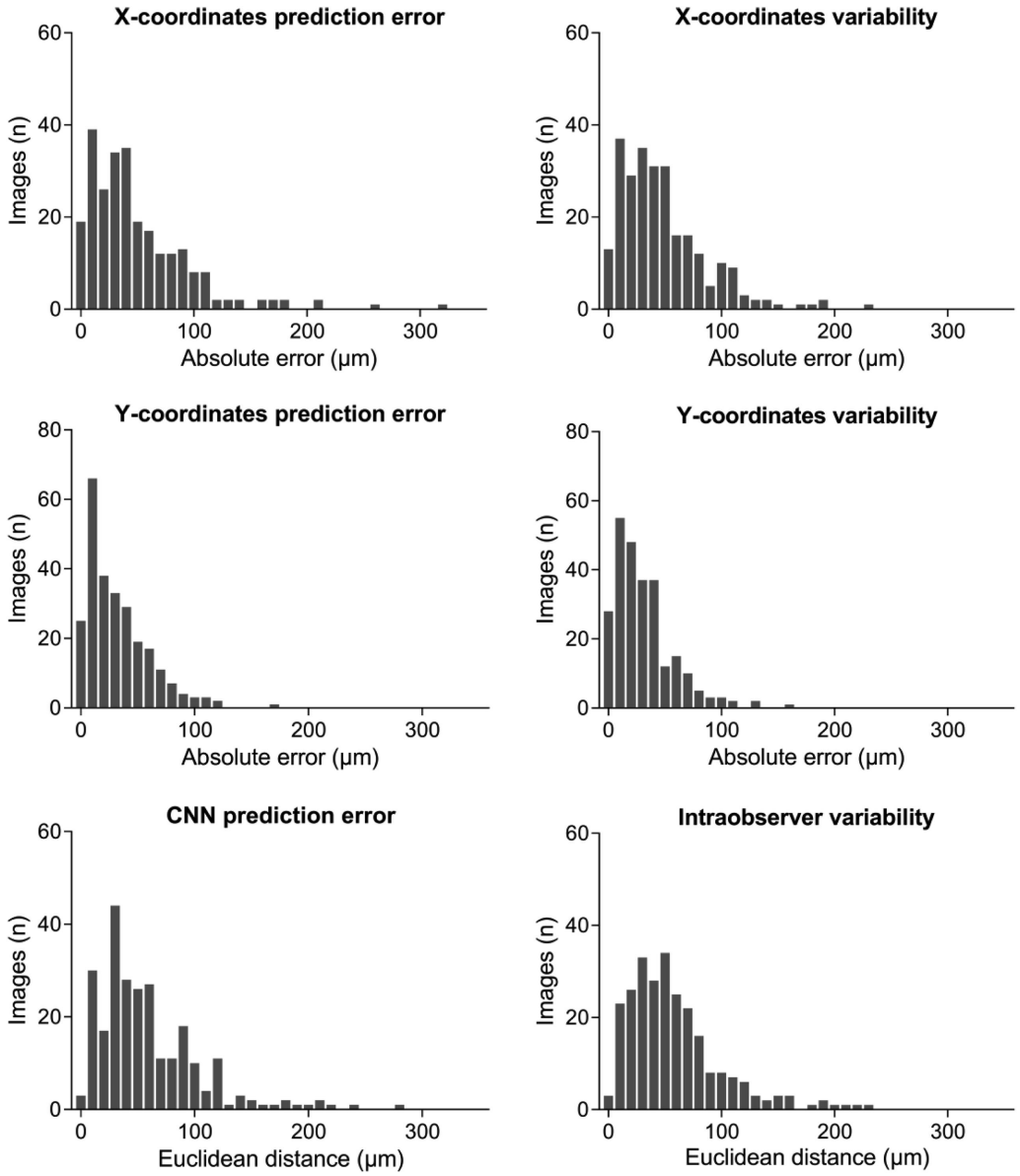

Figure 3. Distribution of CNN prediction error and intraobserver errors. (*TOP*) The distribution of the CNN prediction absolute error (*left*) and intra-observer errors (*right*) for X-coordinates. (*Middle*) The distribution of the CNN prediction absolute error (*left*) and intra-observer errors (*right*) for Y-coordinates. (*Bottom*) The Euclidean distance distribution of the CNN (*left*) and intra-observer (*right*).

Impact of Scleral Spur Location on Angle Parameters

We evaluated the TIA500 and AOD500 calculated using the CNN model predicted scleral spur coordinates and the TIA500 and AOD500 calculated using the reference coordinates as reference values. The mean Euclidean distance between 2 scleral spur locations identified by the expert and CNN was 60.41 ± 49.02 μm. The mean absolute error in TIA500 was 1.26 ± 1.38 degrees for all test images and the mean absolute error in AOD500 was 0.039 ± 0.051 mm. Figure 5 shows the impact of the localization error of the scleral spur on TIA500 and AOD500. When the Euclidean distance increased by 10 μm, the mean absolute error in TIA500 increased by 0.162 degrees and the mean absolute error in AOD500 increased by 0.006 mm.

Discussion

This study developed and tested a deep learning model that detects the scleral spur in UBM images

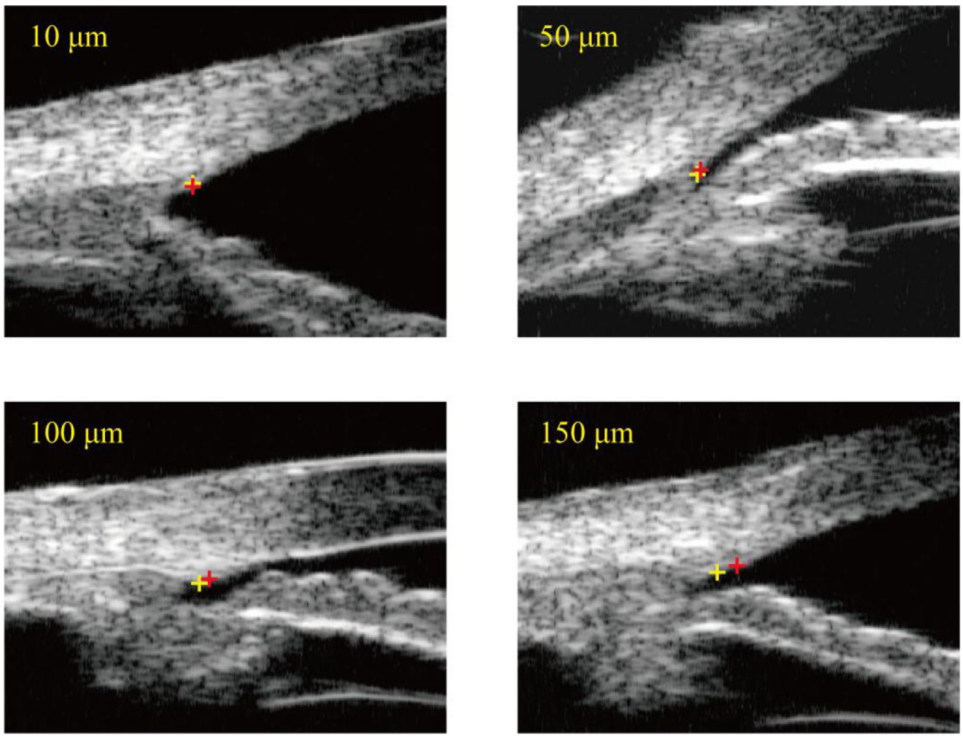

Figure 4. Representative images of various Euclidean distances (10, 50, 100, and 150 µm) between the scleral spur locations marked by the glaucoma specialist (*yellow cross*) and predicted by CNN model (*red cross*).

Table 4. Comparison of the Scleral Spur Localization Errors of the CNN Model in Different Quadrants

Quadrants	No. of Images	Mean Euclidean Distance (µm)
Temporal	82	57.03 ± 47.70
Nasal	75	63.65 ± 48.15
Superior	46	58.90 ± 45.22
Inferior	55	62.62 ± 55.68

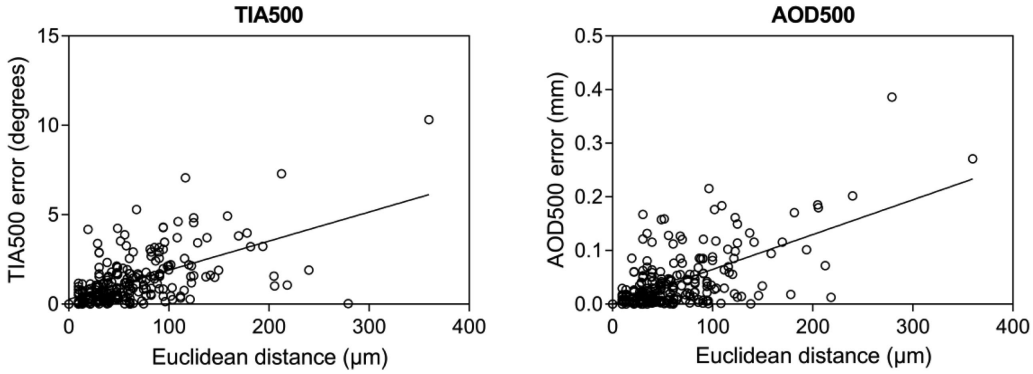

Figure 5. The scleral spur localization error impact on TIA500 (*left*) and AOD500 (*right*).

of open-angle eyes. The CNN was based on the EfficientNetB3 model and achieved localization performance close to that of human experts. We believe that the algorithm has essential implications for automatic quantitative assessment of the opening of the angle and the risk in angle closure.

The ACA is evaluated by gonioscopy, anterior segment optical coherence tomography (AS-OCT), and

UBM in clinical practice.[23,24] UBM can dynamically reflect the morphology of the ACA in the natural state and is more economical than AS-OCT. Therefore, UBM plays a vital role in ACA assessment. Many researchers evaluate ACA automatically based on artificial intelligence. Shi et al. proposed a deep neural network for the automated classification of ACA using UBM images.[15] Fu et al. proposed a CNN for automated angle-closure detection using OCT images.[16] However, most of these studies have carried out qualitative research on ACA, and quantitative research is still limited. The scleral spur is a crucial anatomic landmark for the quantitative assessment of the opening of the angle, such as TIA and AOD. Accurate localization of scleral spur forms the premise of the precise measurement of these parameters.

Automated scleral spur detection has important implications for developing and testing new quantitative methods for automatic quantitative assessment of the opening of the angle. The Zhongshan Angle Assessment Program proposed a semi-automatic measurement method in AS-OCT images[25]; however, their method requires the ophthalmologist first to enter the sclera spur's location. Leung et al. introduced another intuitive approach for measuring TIA based on UBM images.[14] However, the user is still required to enter the scleral spur's location. Our automatic scleral spur localization method forms the basis for automatic quantitative assessment of the opening of the angle. Automating the quantitative analysis of UBM images could also help monitor the progression of angle narrowing and closure over time, which helps diagnose and manage angle-closure glaucoma and other angle-closure diseases.

The intra-observer mean Euclidean distance was 59.78 ± 47.12 µm. This error may be due to the limitations of UBM image resolution or low signal-to-noise ratio in some images in the test set, which affects the specialist's judgment on the scleral spur location. The Euclidean distance calculated by the CNN model was similar to that provided by the specialist, with 85.66% and 95.35% of Euclidean distance within 100 µm and 150 µm of reference scleral spur locations, respectively. Xu et al. studied the localization of the scleral spur based on AS-OCT images.[26] That study reported that a CNN model's distribution of Euclidean distance was 76.22% within 100 µm, compared with 85.33% in our study. However, these results should be interpreted with some caution because their dataset contained angle-closure eyes. In contrast, our study was only based on open-angle eyes, which likely contributed to differences in scleral spur locations' distributions.

The coordinates of the scleral spur predicted by the CNN model were in excellent agreement with those by manual marking. We also assessed our scleral spur localization model's performance by comparing it to the glaucoma specialist's intra-observer variability. The CNN model achieved localization performance close to that of human experts. However, as shown in Table 3, although the CNN model prediction error is very close to the intra-observer variability, the CNN model prediction error is slightly larger than the intra-observer variability. In the future, we may need to increase the number of UBM images in the dataset and continue to optimize the CNN model to achieve better localization performance.

The localization errors of the CNN models in different quadrants showed no statistically significant difference (Mann-Whitney U test, $P > 0.05$), which may be because the anatomic presentation of the scleral spur in different quadrants was basically consistent. Our dataset includes UBM images captured in various directions by multiple examiners. Although we have verified no significant difference in localization errors between each quadrant, UBM is a manually operated device, and UBM images captured by different examiners in different directions may have slight deviations, which may bring potential biases to the results.

In general, the error of TIA500 and AOD500 increases with the increase of Euclidean distance. However, this is not an absolute finding. We found that TIA error and AOD error are close to 0 when the scleral spur localization error exceeds 100 µm in some cases. The scleral spur localization error impact on TIA500 and AOD500 is influenced by angle width and iris morphology to a certain extent. The TIA500 and AOD500 changes may be small if the iris is straightened and has a flat anterior surface.

Our study also had a number of limitations. First, the reference coordinates of the scleral spur were provided only by one glaucoma specialist. Although the specialist has extensive clinical experience, his judgment of the scleral spur's position is subjective. Using the average values of coordinates marked by multiple ophthalmologists as reference coordinates for CNN model training may help improve the model's positioning performance. Second, all UBM images came from the same UBM device. Image size and resolution may differ among UBM devices; as such, this study's research results may not apply to other UBM devices. The use of multiple UBM devices for image acquisition may improve the generalizability of the results.

In summary, we have proposed a deep learning method for the automatic localization of scleral spurs in UBM images of open-angle eyes. The accuracy

of scleral spur localization using this deep learning method is similar to that of glaucoma specialist. We believe that the automatic localization of scleral spur would facilitate the automated quantitative assessment of the opening of the angle and improve the automatic evaluation of PACG risk. These findings will prove to be valuable to future clinical practice.

Acknowledgments

Supported by CAMS Initiative for Innovative Medicine (2017-12M-3-020) and Key technologies R&D program of Tianjin (19YFZCSY00510).

Disclosure: **W. Wang**, None; **L. Wang**, None; **T. Wang**, None; **X. Wang**, None; **S. Zhou**, None; **J. Yang**, None; **S. Lin**, None

References

1. Riva I, Micheletti E, Oddone F, et al. Anterior Chamber Angle Assessment Techniques: A Review. *J Clin Med*. 2020;9:381.
2. Barkana Y, Dorairaj SK, Gerber Y, Liebmann JM, Ritch R. Agreement between gonioscopy and ultrasound biomicroscopy in detecting iridotrabecular apposition. *Arch Ophthalmol*. 2007;125:1331–1335.
3. He M, Friedman DS, Ge J, et al. Laser peripheral iridotomy in primary angle-closure suspects: biometric and gonioscopic outcomes: the Liwan Eye Study. *Ophthalmology*. 2007;114:494–500.
4. Pavlin CJ, Harasiewicz K, Foster FS. Ultrasound Biomicroscopy of Anterior Segment Structures in Normal and Glaucomatous Eyes. *Am J Ophthalmol*. 1992;113:381–389.
5. Foster FS, Pavlin CJ, Harasiewicz KA, Christopher DA, Turnbull DH. Advances in ultrasound biomicroscopy. *Ultrasound Med Biol*. 2000;26:1–27.
6. Shinoj VK, Xue JJH, Murukeshan VM, Baskaran M, Aung T. Progress in anterior chamber angle imaging for glaucoma risk prediction - A review on clinical equipment, practice and research. *Med Eng Phys*. 2016;38:1383–1391.
7. Maslin JS, Barkana Y, Dorairaj SK. Anterior segment imaging in glaucoma: An updated review. *Indian J Ophthalmol*. 2015;63:630–640.
8. Lambiase A, Abdolrahimzadeh B, Calafiore S, Anselmi G, Mannino C, Mannino G. A review of the role of ultrasound biomicroscopy in glaucoma associated with rare diseases of the anterior segment. *Clin Ophthalmol*. 2016;10:1453–1459.
9. Sun X, Dai Y, Chen Y, et al. Primary angle closure glaucoma: What we know and what we don't know. *Prog Retin Eye Res*. 2017;57:26–45.
10. Nongpiur ME, Ku JY, Aung T. Angle closure glaucoma: a mechanistic review. *Curr Opin Ophthalmol*. 2011;22:96–101.
11. Weinreb RN, Aung T, Medeiros FA. The pathophysiology and treatment of glaucoma: a review. *JAMA*. 2014;311:1901–1911.
12. Pavlin CJ, Harasiewicz K, Sherar MD, Foster FS. Clinical use of ultrasound biomicroscopy. *Ophthalmology*. 1991;98:287–295.
13. Pavlin CJ, Harasiewicz K, Foster FS. Ultrasound biomicroscopy of anterior segment structures in normal and glaucomatous eyes. *Am J Ophthalmol*. 1992;113:381–389.
14. Leung CK-S, Yung W-H, Yiu CK-F, et al. Novel approach for anterior chamber angle analysis: anterior chamber angle detection with edge measurement and identification algorithm (ACADEMIA). *Arch Ophthalmol*. 2006;124:1395–1401.
15. Shi G, Jiang Z, Deng G, et al. Automatic Classification of Anterior Chamber Angle Using Ultrasound Biomicroscopy and Deep Learning. *Transl Vis Sci Technol*. 2019;8:25.
16. Fu H, Baskaran M, Xu Y, et al. A Deep Learning System for Automated Angle-Closure Detection in Anterior Segment Optical Coherence Tomography Images. *Am J Ophthalmol*. 2019;203:37–45.
17. Fu H, Li F, Sun X, et al. AGE challenge: Angle Closure Glaucoma Evaluation in Anterior Segment Optical Coherence Tomography. *Med Image Anal*. 2020;66:101798.
18. Long E, Lin H, Liu Z, et al. An artificial intelligence platform for the multihospital collaborative management of congenital cataracts. *Nat Biomed Eng*. 2017;1:0024.
19. Kunimatsu S, Tomidokoro A, Mishima K, et al. Prevalence of appositional angle closure determined by ultrasonic biomicroscopy in eyes with shallow anterior chambers. *Ophthalmology*. 2005;112:407–412.
20. Sunita R, Jovina S, Smith SD, et al. Reproducibility of anterior chamber angle measurements obtained with anterior segment optical coherence tomography. *Invest Ophthalmol Vis Sci*. 2007;48:3683–3688.

21. Pavlin CJ, Foster FS. Ultrasound biomicroscopy in glaucoma. *Acta Ophthalmol Suppl*. 2010;70:7–9.
22. Pavlin CJ, Ritch R, Foster FS. Ultrasound Biomicroscopy in Plateau Iris Syndrome. *Am J Ophthalmol*. 1992;113:390–395.
23. Ursea R, Silverman RH. Anterior-segment imaging for assessment of glaucoma. *Expert Rev Ophthalmol*. 2010;5:59–74.
24. Sarwat S. The Role of Anterior Segment Optical Coherence Tomography in Glaucoma. *J Ophthalmol*. 2012;2012:476801.
25. Console JW, Sakata LM, Aung T, Friedman DS, He M. Quantitative analysis of anterior segment optical coherence tomography images: the Zhongshan Angle Assessment Program. *Br J Ophthalmol*. 2008;92:1612–1616.
26. Xu BY, Chiang M, Pardeshi AA, Moghimi S, Varma R. Deep Neural Network for Scleral Spur Detection in Anterior Segment OCT Images: The Chinese American Eye Study. *Transl Vis Sci Technol*. 2020;9:18.